Research Article

Superresolution under Photometric Diversity of Images

Murat Gevrekci and Bahadir K. Gunturk

Department of Electrical Engineering, Louisiana State University, Baton Rouge, LA 70809, USA

Superresolution (SR) is a well-known technique to increase the quality of an image using multiple overlapping pictures of a scene. SR requires accurate registration of the images, both geometrically and photometrically. Most of the SR articles in the literature have considered geometric registration only, assuming that images are captured under the same photometric conditions. This is not necessarily true as external illumination conditions and/or camera parameters (such as exposure time, aperture size, and white balancing) may vary for different input images. Therefore, photometric modeling is a necessary task for superresolution. In this paper, we investigate superresolution image reconstruction when there is photometric variation among input images.

1. INTRODUCTION

Detailed visual descriptions are demanded in a variety of commercial and military applications, including surveillance systems, medical imaging, and aerial photography. Imaging devices have limitations in terms of, for example, spatial resolution, dynamic range, and noise characteristics. Researchers are working to improve sensor characteristics by exploring new materials, manufacturing processes, and technologies. In addition to the developments in sensor technology, image processing ideas are also explored to improve image quality. One promising research direction is the application of superresolution image reconstruction, where multiple images are combined to improve spatial resolution. Super resolution (SR) algorithms exploit information diversity among overlapping images through subpixel image registration. Accuracy of subpixel registration allows us to obtain frequency components that are unavailable in individual images. The idea of SR image reconstruction has been investigated extensively, and commercial products are becoming available [1, 2]. For detailed literature surveys on SR, we refer the readers to other sources [3–7].

In this paper, we focus on a new issue in SR: how to perform SR when some of the input images are photometrically different than the others? Other than a few recent papers, almost all SR algorithms in the literature assume that input images are captured under the same photometric conditions. This is not necessarily true in general. External illumination conditions may not be identical for each image. Images may be captured using different cameras that have different radiometric response curves and settings (such as exposure time and ISO settings). Even if the same camera is used for all images, camera parameters (exposure time, aperture size, white balancing, gain, etc.) may differ from one image to another. (Almost all modern cameras have automatic control units adjusting the camera parameters. Low-end "point-and-shoot" digital cameras determine these parameters based on some built-in algorithms and do not allow users to change them. A slight repositioning of the camera or a change in the scene may result in a different set of parameters.) Therefore, an SR algorithm should include a photometric model as well as a geometric model and incorporate these models in the reconstruction.

For accurate photometric modeling, the camera response function (CRF) and the photometric camera settings should be taken into account. The CRF, which is the mapping between the irradiance at a pixel to the output intensity, is not necessarily linear. Charges created at a pixel site due to incoming photons may exceed the holding capacity of that site. When the amount of charge at a pixel site approaches the saturation level, the response may deviate from a linear response. When a pixel site saturates, it outputs the same intensity even if more photons come in. (If photons keep coming after saturation, the charge starts to fill the neighboring pixels unless there is an antiblooming technology in the sensor.) In addition, camera manufacturers may also introduce

intentional nonlinearity to CRF to improve contrast and visual quality.

The CRF saturation and the finite number of bits (typically eight bits per channel) to represent a pixel intensity limit the resolution and the extent of the dynamic range that can be captured by a digital camera. Because a real scene typically has much wider dynamic range than a camera can capture, an image captures only a limited portion of the scene's dynamic range. By changing exposure rate, it is possible to get information from different parts of a scene. In high-dynamic-range (HDR) imaging research, multiple low-dynamic-range (LDR) images (that are captured with different exposure rates) are combined to produce an HDR image [8–11]. This process requires estimation or knowledge of the exposure rates and CRF. Spatial registration, lens flare, ghost removal, vignetting correction, compression, and display of HDR images are some of the other challenges in HDR imaging.

Despite the likelihood of photometric variations among images of a scene, there are few SR papers addressing reconstruction with such image sets. In [5, 12], photometric changes were modeled as global gain and offset parameters among image intensities. This is a successful model when photometric changes are small. When photometric changes are large, nonlinearity of CRF should be taken into consideration. In [13], we included a nonlinear CRF model in the imaging process, and proposed an SR algorithm based on the maximum a posteriori probability estimation technique. The algorithm produces the high-resolution irradiance of the scene; it requires estimation of the CRF and its inverse explicitly. The algorithm derives a specific *certainty function* using the Taylor series expansion of the inverse of the CRF. (As we will see, certainty function controls the contribution of each pixel in reconstruction. It gives less weight to noisy and saturated pixels than reliable pixels. It is necessary for a good reconstruction performance.)

In this paper, we propose an alternative method. The method works in the intensity domain instead of the irradiance domain as proposed in [13]. It is not necessary to estimate the CRF or the camera settings; intensity-to-intensity mapping is sufficient. The spatial resolution of the reference image is enhanced without going to the irradiance domain. In addition, the photometric weight function is generic in the derivations; no Taylor series expansion is required.

The rest of the paper is as follows. In Section 2, we compare two photometric models that have been applied in SR. We show that nonlinear photometric modeling is necessary when photometric changes are significant. (This is also an important contribution of the paper.) We then investigate two possible approaches for SR under photometric diversity in Section 3. In Section 4, we explain how geometric and photometric registrations among images are achieved. We provide experimental results with real data sets in Section 5. Conclusions and future work are given in Section 6.

2. PHOTOMETRIC MODELING

For a complete SR algorithm, spatial and photometric processes of an imaging system should be modeled. Spatial processes (spatial motion, sampling, point spread function) have been investigated relatively well; here, we investigate photometric modeling. As mentioned earlier, in the context of SR, two photometric models have been used. The first one is the affine model used in [5, 12], and the second one is the nonlinear model used in [13]. In this section, we review and compare these two models.

2.1. Affine photometric model

Suppose that N images of a static scene are captured and these images are geometrically registered. Let $\mathbf{q}$ be the irradiance of the scene, and let $\mathbf{z}_i$ be the ith measured image.[1] According to the affine model, the relation between the irradiance and the image is as follows:

$$\mathbf{z}_i = a_i\mathbf{q} + b_i, \quad i = 1,\ldots,N, \tag{1}$$

where the gain (a_i) and offset (b_i) parameters can model a variety of things, including global external illumination changes and camera parameters such as gain, exposure rate, aperture size, and white balancing. (In HDR image construction from multiple exposures, only the exposure rate is manually changed, keeping the rest of the camera parameters fixed [8]. In such a case, the offset term can be neglected.) Then, the ith and the jth images are related to each other as follows:

$$\mathbf{z}_j = a_j\mathbf{q} + b_j = a_j\left(\frac{\mathbf{z}_i - b_i}{a_i}\right) + b_j = \frac{a_j}{a_i}\mathbf{z}_i + \frac{a_ib_j - a_jb_i}{a_i}. \tag{2}$$

Defining $\alpha_{ji} \equiv a_j/a_i$ and $\beta_{ji} \equiv (a_ib_j - a_jb_i)/a_i$, we can in short write (2) as

$$\mathbf{z}_j = \alpha_{ji}\mathbf{z}_i + \beta_{ji}. \tag{3}$$

The affine relation given in (3) is used in [12] to model photometric changes among the images to be used in SR reconstruction. In [12], the images are first geometrically registered to the reference image to be enhanced. (A feature-based registration method is used. Corner points in the images are extracted and matched using normalized cross-correlation. Perspective registration parameters are estimated after outlier rejection.) After geometric registration, the relative gain and offset terms with respect to the reference image are calculated with least-squares estimation. Each image is photometrically corrected using the gain and offset terms. This is followed by SR reconstruction.

Although the affine transformation in (3) can handle small photometric changes, the conversion accuracy decreases drastically in case of large changes. This is why in HDR imaging, nonlinear photometric modeling is preferred over affine modeling.

2.2. Nonlinear photometric model

A typical image sensor has a nonlinear response to the amount of light it receives. Estimation of nonlinear camera

---

[1] In our formulations, images are represented as column vectors.

response function (CRF) becomes crucial in a variety of applications, including HDR imaging, panoramic image construction [14, 15], photometric stereo [16], bidirectional reflectance distribution function (BRDF) estimation, and thermography.

According to the nonlinear photometric model, an image $\mathbf{z}_i$ is related to the irradiance $\mathbf{q}$ of the scene as follows:

$$\mathbf{z}_i = f(a_i\mathbf{q} + b_i), \tag{4}$$

where $f(\cdot)$ is the camera response function (CRF), and a_i and b_i are again the gain and offset parameters as in (1). Then, two images are related to each other as follows:

$$\mathbf{z}_j = f\left(\frac{a_j}{a_i}f^{-1}(\mathbf{z}_i) + \frac{a_ib_j - a_jb_i}{a_i}\right) = f(\alpha_{ji}f^{-1}(\mathbf{z}_i) + \beta_{ji}). \tag{5}$$

The function $f(\alpha_{ji}f^{-1}(\cdot) + \beta_{ji})$ is known as the intensity mapping function (IMF). (Note that in some papers such as [17], the offset term in the above equation is neglected and the term $f(\alpha_{ji}f^{-1}(\cdot))$ is called the IMF.) Although IMF can be constructed using CRF and exposure ratios, it is not necessary to estimate camera parameters to find IMF. IMF can be extracted directly from the histograms of the images [17]. Another way to estimate IMF is proposed in [18], which estimates IMF from two-dimensional intensity distribution of input images. Slenderizing this joint intensity distribution results in IMF. Reference [18] also estimates the CRF and exposure rates using a nonlinear optimization technique. CRF can also be estimated without finding IMF. In [19], a parametric CRF model is proposed; and these parameters are estimated iteratively. Reference [20] uses a polynomial model instead of a parametric model. In [9], a nonparametric CRF estimation technique with a regularization term is presented. Another nonparametric CRF estimation method is proposed in [21], which also includes modeling of noise characteristics.

2.3. Comparison of photometric models

Here, we provide an example to compare affine and nonlinear photometric models. In Figures 1(a), 1(b), 1(c), 1(d), we provide four images captured with a handheld digital camera. One of the images is set as the reference image (Figure 1(d)) and the others are converted to it photometrically using the affine and nonlinear models. (Before photometric conversion, images were registered geometrically.) The residual images computed using the affine model (Figures 1(e), 1(f), 1(g)) and the nonlinear model (Figures 1(i), 1(j), 1(k)) are displayed. The affine model parameters are estimated using the least-squares technique and are shown in Figure 1(h). The nonlinear IMFs are estimated using the method in [22]. The estimated mappings are shown in Figure 1(l). As seen from the residual images, the nonlinear model works better than the affine model. The affine model performs well when the exposure ratios are close; the model becomes more and more insufficient as the exposure ratios differ more. Figure 2 demonstrates this for a larger set of exposure ratios, ranging from 2 to 50.

A superresolution algorithm requires an accurate modeling of the imaging process. The restored image should be consistent with the observations given the imaging model. A typical iterative SR algorithm (POCS-based [23], Bayesian [24], iterated back-projection [25]) starts with an initial estimate, calculates an observation using the imaging model, finds the residual between the calculated and real observations, and projects the residual back onto the initial estimate. When the imaging model is not accurate or registration parameters are not estimated correctly, the algorithm would fail. In this section, we conclude that nonlinear photometric models should be a part of SR algorithms when there is a possibility of photometric diversity among input images.

3. SR UNDER PHOTOMETRIC DIVERSITY

When all input images are not photometrically identical, there are two possible ways to enhance a reference image: (i) spatial resolution enhancement and (ii) spatial resolution and dynamic range enhancement. In (i), only spatial resolution of the reference image is improved. This requires photometric mapping of all input data to the reference image. In (ii), both spatial resolution and dynamic range of the reference image are improved. This can be considered as a combination of high-dynamic-range imaging and superresolution image restoration.

3.1. Spatial resolution enhancement

In spatial resolution enhancement, all input images are converted to the tonal range of reference image. After photometric registration, a traditional SR reconstruction algorithm can be applied. However, this is not a straightforward process when the intensity mapping is nonlinear. Refer to Figure 3 that shows various intensity mapping functions (IMFs). Suppose that $\mathbf{z}_1$ is the reference image to be enhanced. Input image $\mathbf{z}_2$ is photometrically mapped onto $\mathbf{z}_1$ in all cases. There are four cases in Figure 3.

(i) In case (a), the input image $\mathbf{z}_2$ has the same photometric range with the reference image; so there is no photometric registration necessary.

(ii) In case (b), the IMF is nonlinear; however, there is no saturation. Therefore, the intensities of $\mathbf{z}_2$ can be mapped onto the range of $\mathbf{z}_1$ using the IMF without loss of information.

(iii) In case (c), there is bright saturation in $\mathbf{z}_2$. The IMF is not a one-to-one mapping. The problematic region is where the slope of the IMF is zero or close to zero. For saturated regions, there is no information in $\mathbf{z}_2$ corresponding to $\mathbf{z}_1$. Therefore, perfect photometric mapping from $\mathbf{z}_2$ to $\mathbf{z}_1$ is not possible. When additive sensor noise and quantization are considered, small-slope (referring to the slope of the IMF) regions would also be problematic in addition to the zero-slope (saturation) regions. In these regions, noise and quantization error in $\mathbf{z}_2$ would be amplified when mapped onto $\mathbf{z}_1$, and reconstruction would be affected negatively.
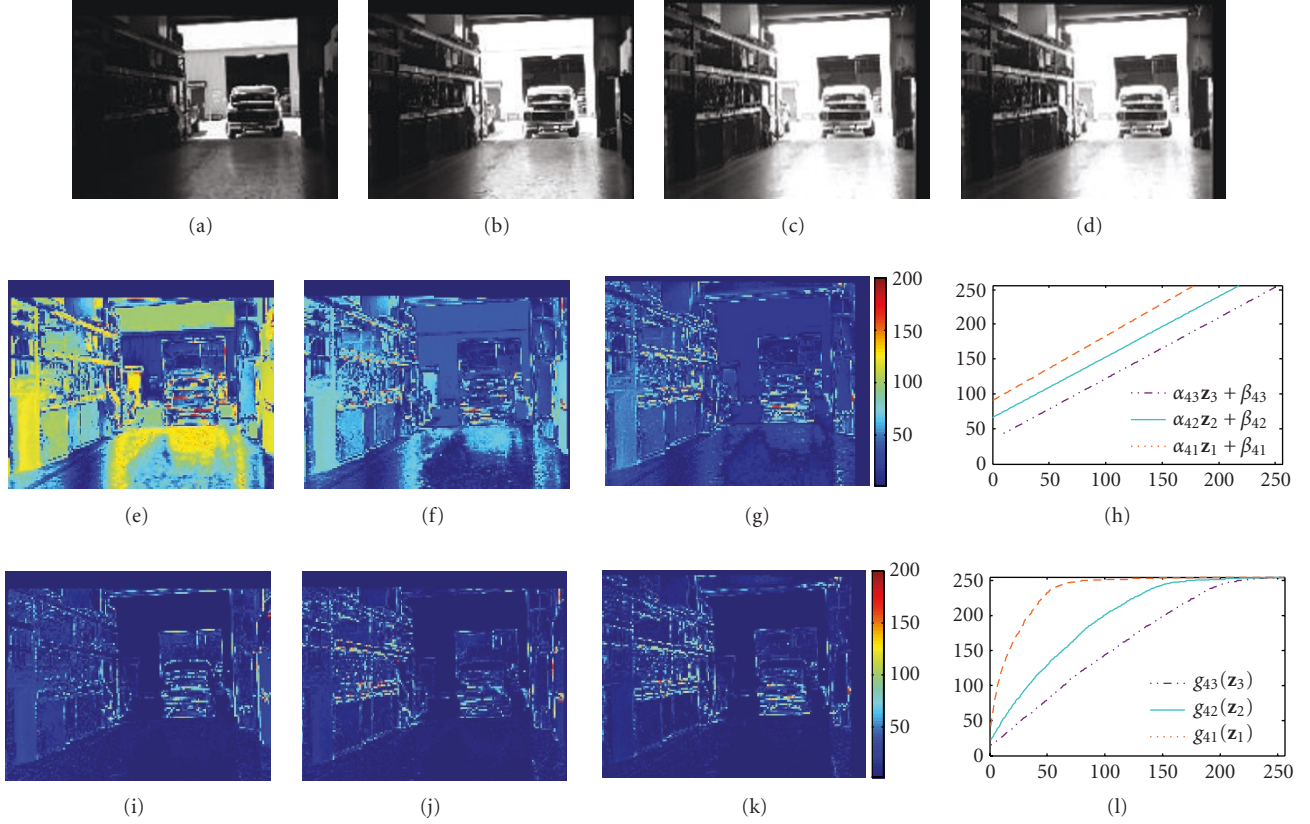
FIGURE 1: Comparison of affine and nonlinear photometric conversions. (a)–(d) are the images captured with different exposure rates. All camera parameters other than the exposure rates are fixed. The images are geometrically registered. The relative exposure rates are as follows: (a) image $\mathbf{z}_1$ with exposure rate 1/16; (b) image $\mathbf{z}_2$ with exposure rate 1/4; (c) image $\mathbf{z}_3$ with exposure rate 1/2; (d) image $\mathbf{z}_4$ with exposure rate 1. Image $\mathbf{z}_4$ is set as the reference image and other images are photometrically registered to it. The residuals and the registration parameters are shown; (e) residual between $\mathbf{z}_4$ and photometrically aligned $\mathbf{z}_1$ using the affine model; (f) residual between $\mathbf{z}_4$ and photometrically aligned $\mathbf{z}_2$ using the affine model; (g) residual between $\mathbf{z}_4$ and photometrically aligned $\mathbf{z}_3$ using the affine model; (h) the photometric mappings for (e)–(g); (i) residual between $\mathbf{z}_4$ and photometrically aligned $\mathbf{z}_1$ using the nonlinear model; (j) residual between $\mathbf{z}_4$ and photometrically aligned $\mathbf{z}_2$ using the nonlinear model; (k) residual between $\mathbf{z}_4$ and photometrically aligned $\mathbf{z}_3$ using the nonlinear model; (l) the photometric mappings for (i)–(k).

(iv) In case (d), there are regions of small slope and large slope. Large-slope regions are not an issue because mapping from $\mathbf{z}_2$ to $\mathbf{z}_1$ would not create any problem. The problem is still with the small-slope regions (dark saturation regions in $\mathbf{z}_2$), where quantization error and noise are effective.

One solution to the saturation and noise amplification problems is to use a certainty function associated with each image. The certainty function should weight the contribution of each pixel in reconstruction based on the reliability of conversion. If a pixel is saturated or close to saturation, then the certainty function should be close to zero. If a pixel is from a reliable region, then the certainty function should be close to one. The issue of designing a certainty function has been investigated in HDR research. In [22], the certainty function is defined according to the derivative of the CRF. The motivation is that for pixels corresponding to low-slope regions of the CRF, the reliability should also be low. In [13], the certainty function includes variances of the additive noise and

quantization errors in addition to the derivative of the CRF. In [9], a fixed hat function is used. According to it, the mid-range pixels have high reliability, while low-end and high-end pixels have low reliability.

We now put these ideas in SR reconstruction. Let $\mathbf{x}$ be the (unknown) high-resolution version of a reference image $\mathbf{z}_r$, and define $g_{ri}(\mathbf{z}_i)$ as the IMF that takes $\mathbf{z}_i$ and converts it to the photometric range of $\mathbf{z}_r$ (therefore, $\mathbf{x}$). Referring to (5), $g_{ri}(\mathbf{z}_i)$ includes the CRF $f(\cdot)$, and gain α_{ri}, and offset β_{ri} parameters:

$$g_{ri}(\mathbf{z}_i) \equiv f(\alpha_{ri} f^{-1}(\mathbf{z}_i) + \beta_{ri}). \tag{6}$$

We also need to model spatial transformations of the imaging process. Define $\mathbf{H}_i$ as the linear mapping that takes a high-resolution image and produces a low-resolution image. $\mathbf{H}_i$ includes motion (of the camera or the objects in the scene), blur (caused by the point spread function of the sensor elements and the optical system), and downsampling. (Details of $\mathbf{H}_i$ modeling can be found in the special issue of
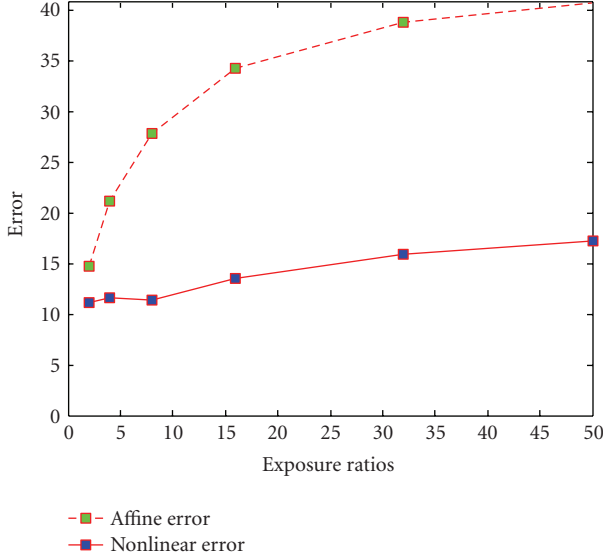
FIGURE 2: Root-mean-square error (RMSE) values of photometrically registered images with relative exposure rates of 2, 4, 8, 16, 32, 50. The RMSE values (green points) for affine mappings are 14.8, 21.1, 27.8, 34.3, 38.7, 40.7. The RMSE values (blue points) for nonlinear mappings are 11.2, 11.6, 11.4, 13.5, 15.9, 17.2.

the IEEE Signal Processing Magazine [3] and the references therein.)

When $\mathbf{H}_i$ is applied on $\mathbf{x}$, it should produce the photometrically converted ith observation, $g_{ri}(\mathbf{z}_i)$. That is, we need to find $\mathbf{x}$ that produces $g_{ri}(\mathbf{z}_i)$ when $\mathbf{H}_i$ is applied to it, for all i. The least-squares solution to this problem would minimize the following cost function:

$$C(\mathbf{x}) = \sum_i \left\| g_{ri}(\mathbf{z}_i) - \mathbf{H}_i\mathbf{x} \right\|^2. \tag{7}$$

As explained earlier, the problem associated with the saturation of the IMF can be solved using a certainty function, $w(\mathbf{z}_i)$. We formulate our equations using a generic function $w(\mathbf{z}_i)$. Our specific choice will be given in the experimental results Section 5. We now define a diagonal matrix $\mathbf{W}_i$ whose diagonal is $w(\mathbf{z}_i)$, and incorporate this matrix into (7) to find the weighted least-squares solution. The new cost function is

$$C(\mathbf{x}) = \frac{1}{2} \sum_i \left(g_{ri}(\mathbf{z}_i) - \mathbf{H}_i\mathbf{x} \right)^T \mathbf{W}_i \left(g_{ri}(\mathbf{z}_i) - \mathbf{H}_i\mathbf{x} \right). \tag{8}$$

Since dimensions of the matrices are large, we want to avoid matrix inversion and apply the gradient descent technique to find $\mathbf{x}$ that minimizes this cost function. Starting with an initial estimate $\mathbf{x}^{(0)}$, each iteration updates $\mathbf{x}^{(0)}$ in the direction of the negative gradient of $C(\mathbf{x})$:

$$\mathbf{x}^{(k+1)} = \mathbf{x}^{(k)} + \gamma \sum_i \mathbf{H}_i^T \mathbf{W}_i \left(g_{ri}(\mathbf{z}_i) - \mathbf{H}_i\mathbf{x}^{(k)} \right), \tag{9}$$

where γ is the step size at the kth iteration. Defining $\mathbf{\Phi}$ as the negative gradient of $C(\mathbf{x})$, the exact line search that minimizes $C(\mathbf{x}^{(k)} + \gamma\mathbf{\Phi})$ yields the step size:

$$\gamma = \frac{\mathbf{\Phi}^T\mathbf{\Phi}}{\mathbf{\Phi}^T\left[\sum_i \mathbf{H}_i^T\mathbf{W}_i\mathbf{H}_i\right]\mathbf{\Phi}}, \tag{10}$$

with

$$\mathbf{\Phi} = \sum_i \mathbf{H}_i^T\mathbf{W}_i\left(g_{ri}(\mathbf{z}_i) - \mathbf{H}_i\mathbf{x}^{(k)}\right). \tag{11}$$

An iteration of the algorithm is illustrated in Figure 4, and the pseudocode is given in Algorithm 1. Note that in implementation, it is not necessary to construct matrices or vectors to follow the steps of the algorithm. Application of $\mathbf{H}_i$ can be implemented as warping an image geometrically, convolving with the point spread function (PSF), and downsampling. Similarly, $\mathbf{H}_i^T$ can be implemented as upsampling with zero insertion, convolving with a flipped PSF, and back-warping [13]. The step size γ can be obtained using the same principles.

3.2. Spatial resolution and dynamic range enhancement

Here, the goal is to produce a high-resolution and high-dynamic range image. One option is to obtain the high-resolution version of each input image using the algorithm given in Algorithm 1, and then apply HDR image construction to these high-resolution images.

A second option is to derive the high-resolution irradiance $\mathbf{q}$ directly. This requires formulating the image acquisition from the unknown high-resolution irradiance $\mathbf{q}$ to each observation $\mathbf{z}_i$. Adding the spatial processes (geometric warping, blurring with the PSF, and downsampling) to (4), the imaging process can be formulated as

$$\mathbf{z}_i = f\left(a_i\mathbf{H}_i\mathbf{q} + b_i\right), \tag{12}$$

where $\mathbf{H}_i$ is the linear mapping (including warping, blurring, and downsampling operations) from a high-spatial-resolution irradiance signal to a low-spatial-resolution irradiance signal. $f(\cdot)$, a_i, and b_i are the CRF, gain, and offset terms as in (4).

This time, the weighted least-squares estimate of $\mathbf{q}$ minimizes the following cost function:

$$C(\mathbf{q}) = \frac{1}{2} \sum_i \left(\frac{f^{-1}(\mathbf{z}_i) - b_i}{a_i} - \mathbf{H}_i\mathbf{q} \right)^T \mathbf{W}_i \left(\frac{f^{-1}(\mathbf{z}_i) - b_i}{a_i} - \mathbf{H}_i\mathbf{q} \right). \tag{13}$$

This cost function is basically analogous to the cost function in (8). Starting with an initial estimate for $\mathbf{q}$, the rest of algorithms work similar to the one in Algorithm 1. The only difference is that intensity-to-intensity mapping $g_{ri}(\cdot)$ in (8) is replaced with intensity-to-irradiance mapping $(f^{-1}(\cdot) - b_i)/a_i$. Unlike the intensity-to-intensity mapping, intensity-to-irradiance mapping requires explicit estimation of the CRF, gain, and offset parameters.
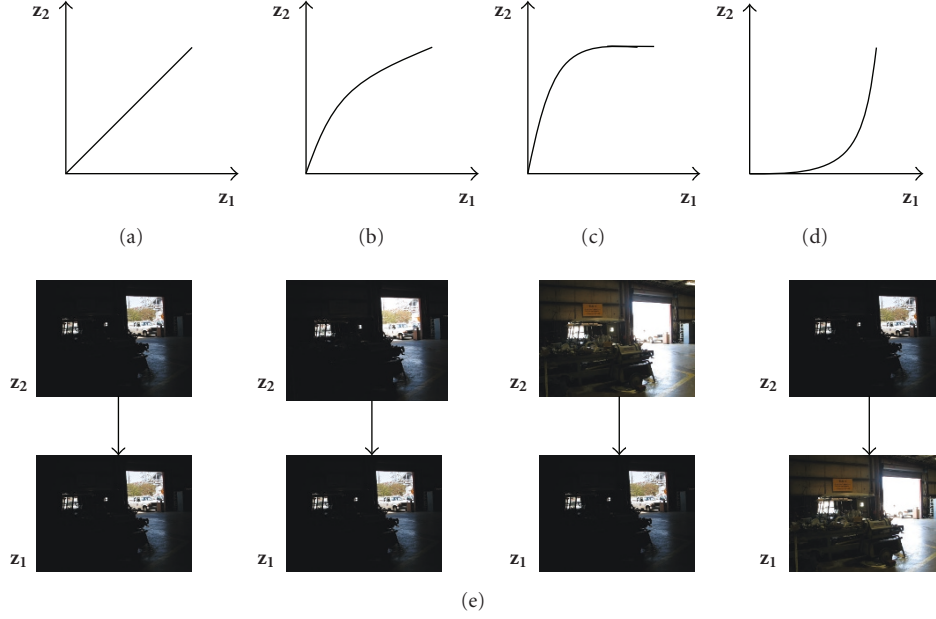
Figure 3: Various photometric conversion scenarios. First row illustrates possible photometric conversion functions. Second and third rows show example images with such photometric conversion.
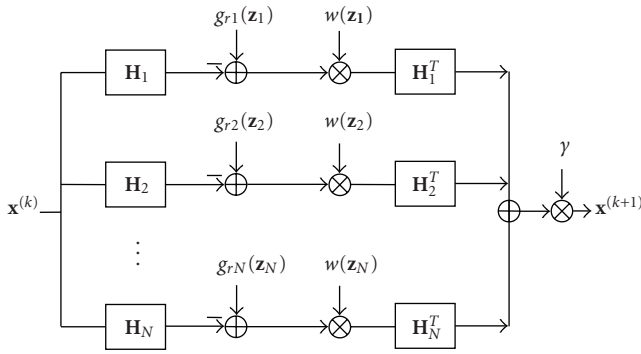

Figure 4: Spatial resolution enhancement framework using IMF. $g_{ri}(\cdot)$ is the IMF that converts input image $\mathbf{z}_i$ to the photometric range of reference image. $\mathbf{H}_i$ applies spatial transformations, consisting of geometric warping, blurring, and downsampling. Similarly, $\mathbf{H}_i^T$ applies upsampling with zero insertion, blurring, and back-warping. γ is the step size of the update; it is computed at each iteration.

We write the iterative step to estimate $\mathbf{q}$ as follows:

$$\mathbf{q}^{(k+1)} = \mathbf{q}^{(k)} + \gamma \sum_i \mathbf{H}_i^T \mathbf{W}_i \left(\frac{f^{-1}(\mathbf{z}_i) - b_i}{a_i} - \mathbf{H}_i \mathbf{q}^{(k)} \right), \quad (14)$$

where γ is the step size. It is obtained similar to the one in (9). The details of this approach are trivial given the derivations in the previous section; therefore, we leave it to the reader.

In [13], we also investigated this joint spatial and dynamic range enhancement idea. The approach in [13] is similar to the one (irradiance-domain solution) given in this section. As we mentioned in Section 1, in [13], we applied

Taylor series expansion to the inverse of the CRF to end up with a specific certainty function. The algorithm requires estimation of the CRF and the variances of noise and quantization error. It also includes a spatial regularization term in the reconstruction. We refer the readers to [13] for details. The derivation in this section can be considered as a generalization of the solution given in [13]; here, the certainty function is not specified. In practice, the method in [13] and the irradiance-domain solution of this section work similarly with the proper selection of certainty functions.

Note that this approach estimates the irradiance $\mathbf{q}$, which needs to be compressed in dynamic range to display on limited dynamic range displays. Displaying HDR images on limited dynamic-range displays is an active research area [26].

3.3. Certainty function

As we have discussed in Section 3.1, the information coming from low-end and high-end of the intensity range is not reliable due to noise, quantization, and saturation. If used, these unreliable pixels would degrade the restoration. In [9], a generalized hat function is proposed to reduce the effect of unreliable pixels. We use a piecewise linear certainty function in our experiments. The certainty function is shown in Figure 5. The intensity breakpoints in the certainty function are 15 and 240, and they were determined by trial and error.

Figure 6 shows an example to demonstrate the reliability of pixels and the effect of the certainty function. The first row in the figure shows photometric conversion from an over-exposed image to an underexposed image. This is the scenario in Figure 3(c). Figure 6(a) is the reference image, and Figure 6(b) is the geometrically warped input image which

(1) Requirements:
- • Set or estimate the point spread function (PSF) of the camera: $\mathbf{h}$
- • Set the resolution enhancement factor: F
- • Set the number of iterations: K

(2) Initialization:
- • Choose the reference image $\mathbf{z}_r$
- • Interpolate $\mathbf{z}_r$ by the enhancement factor F to obtain $\mathbf{x}^{(0)}$

(3) Parameter estimation:
- • Estimate the spatial registration parameters between $\mathbf{z}_r$ and $\mathbf{z}_i$, $i = 1, \ldots, N$
- • Estimate the IMFs, $g_{ri}(\mathbf{z}_i)$, between $\mathbf{z}_r$ and $\mathbf{z}_i$, $i = 1, \ldots, N$

(4) Iterations:
- • For $k = 0$ to $K - 1$
  - • Create a zero-filled initial image $\boldsymbol{\Psi}$ with the same size as $\mathbf{x}^{(0)}$
  - • For $i = 1$ to N
    - • Find $\mathbf{H}_i \mathbf{x}^{(k)}$ with the following steps:
      - • Convolve $\mathbf{x}^{(k)}$ with the PSF $\mathbf{h}$
      - • Warp and downsample the convolved image onto the input $\mathbf{z}_i$
    - • Find the residual $g_{ri}(\mathbf{z}_i) - \mathbf{H}_i \mathbf{x}^{(k)}$
    - • Find the weight image $w(\mathbf{z}_i)$ and multiply it pixel by pixel with the residual $g_{ri}(\mathbf{z}_i) - \mathbf{H}_i \mathbf{x}^{(k)}$
    - • Obtain $\mathbf{H}_i^T \mathbf{W}_i g_{ri}(\mathbf{z}_i) - \mathbf{H}_i \mathbf{x}^{(k)}$ with the following steps:
      - • Upsample the weighted residual by the factor F with zero insertion
      - • Convolve the result with the flipped PSF $\mathbf{h}$
      - • Warp the result to the coordinates of $\mathbf{x}^{(k)}$
    - • Update $\boldsymbol{\Psi}$: $\boldsymbol{\Psi} \leftarrow \boldsymbol{\Psi} + \mathbf{H}_i^T \mathbf{W}_i (g_{ri}(\mathbf{z}_i) - \mathbf{H}_i \mathbf{x}^{(k)})$
  - • Calculate γ
  - • Update the current estimate: $\mathbf{x}^{(k+1)} = \mathbf{x}^{(k)} + \gamma \boldsymbol{\Psi}$

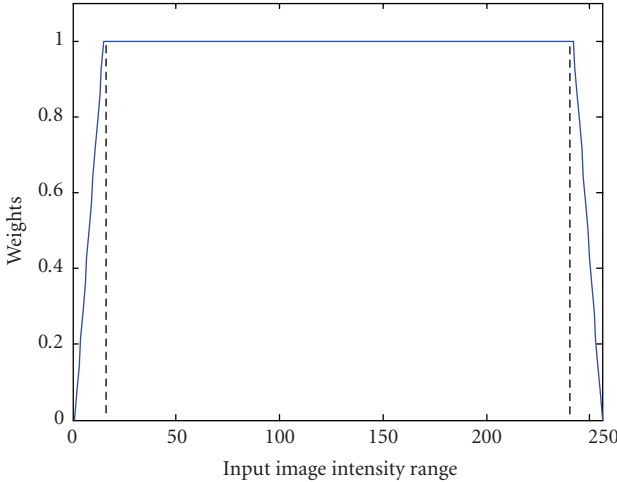ALGORITHM 1: Pseudocode of the spatial enhancement algorithm.

FIGURE 5: Piecewise linear certainty function used in the experiments. The intensity breakpoints in the figure are 15 and 240.

we want to map onto the reference image tonally. Figure 6(c) shows the residual between the input and the reference images without photometric registration. Figure 6(d) shows the residual after the application of IMF to the input image. Clearly, saturated pixels are not handled well: residuals for these pixels are large. The weights for each pixel in the image are calculated with application of the certainty function on the input image; they are shown in Figure 6(e). Examining Figures 6(d) and 6(e), it can be seen that the weights for unreliable saturated pixels are low, as expected. Figure 6(f) shows the final residual after the application of the weight image (Figure 6(e)) on the residual image (Figure 6(d)).

The second row in Figure 6 shows an example of tonal conversion from an underexposed image to an overexposed image. This is the scenario in Figure 3(d). Figure 6(g) is the reference image and Figure 6(h) is the geometrically warped input image. Here, photometric transformation can be performed without any problem for high-end of intensity range. The problem is the low-end, dark saturation regions in the input image. Figure 6(j) shows the residual after tonal conversion. Figure 6(k) is the certainty image. As seen, the unreliable dark saturation regions are having low weights. Figure 6(l) shows the weighted residual obtained by multiplying the residual image with the corresponding certainty image. In the weighted residual image, large residual values (that would degrade SR reconstruction) are eliminated or reduced significantly.

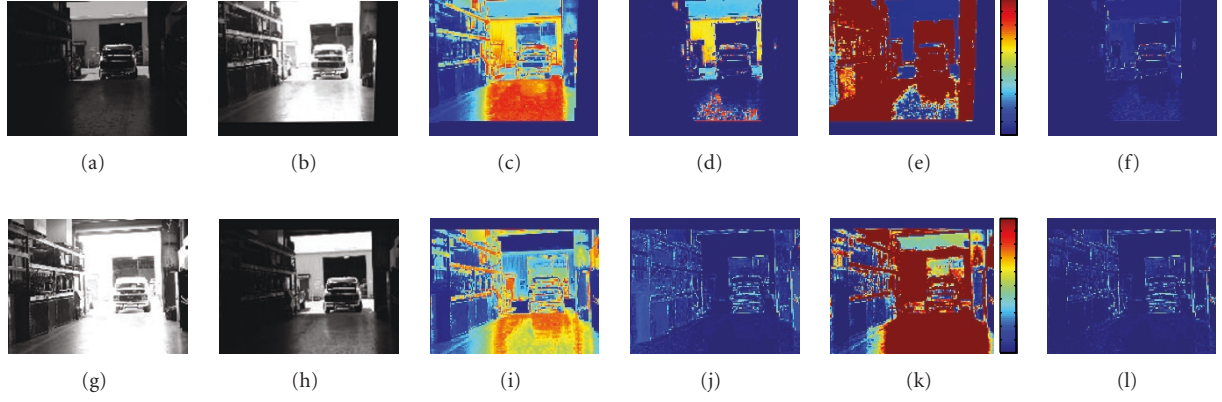| (a) | (b) | (c) | (d) | (e) | (f) |

| (g) | (h) | (i) | (j) | (k) | (l) |

FIGURE 6: Weighting function effect on residuals. First row performs conversion onto low-exposure reference while second row has a reference with high exposure: (a) reference image; (b) geometrically warped input image; (c) residual image without tonal conversion; (d) residual image using nonlinear tonal conversion; (e) certainty image using hat function as weighting and image (b) as input; (f) weighted residual obtained multiplying residual image in (d) by certainty image in (e); (g) reference image; (h) geometrically warped input image; (i) residual image without tonal conversion; (j) residual image using nonlinear tonal conversion; (k) certainty image using hat function as weighting and image (g) as input; (l) weighted residual obtained multiplying residual image in (j) by certainty image in (k).

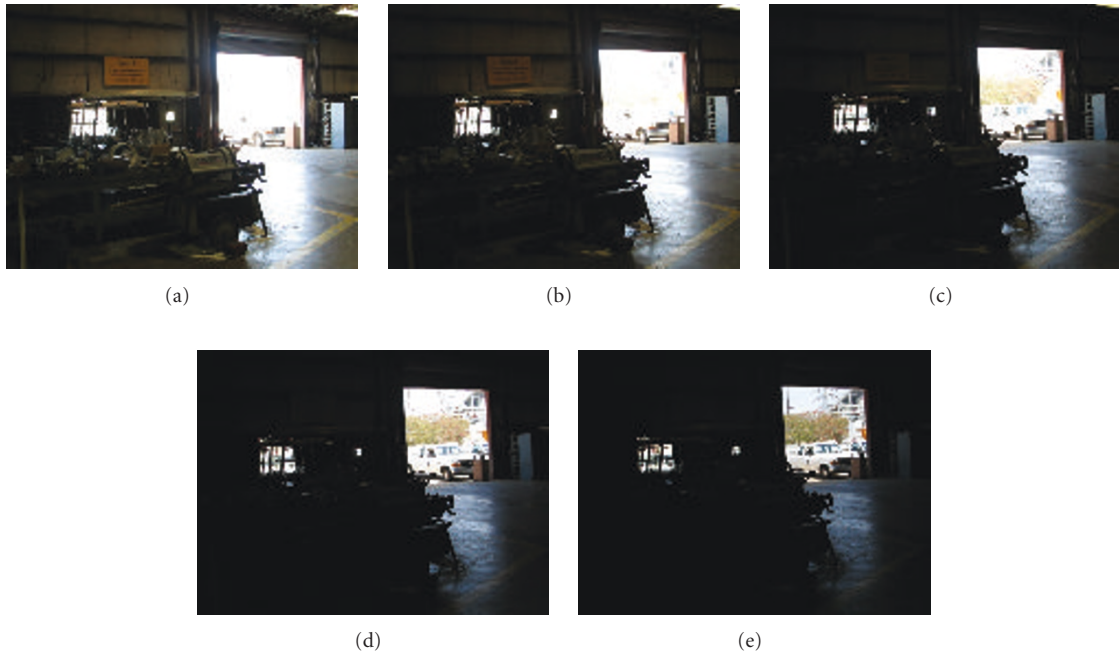
| (a) | (b) | (c) |

| (d) | (e) |

FIGURE 7: Five images of "Facility I" data set that includes 22 images are displayed here. Exposure durations of (a)–(e) are 1/25, 1/50, 1/100, 1/200, and 1/400 seconds, respectively.

4. GEOMETRIC AND PHOTOMETRIC REGISTRATIONS

SR requires accurate geometric and photometric registrations. If the actual CRF and the exposure rates are unknown, the images must be geometrically registered before these parameters can be estimated. On the other hand, geometric registration is problematic when images are not photometrically registered. There are three possible approaches to this problem.

(A1) Images are first geometrically registered using an algorithm that is insensitive to photometric changes. This is followed by photometric registration.

(A2) Images are first photometrically registered using an algorithm that is insensitive to geometric misalignments. This is followed by geometric registration.

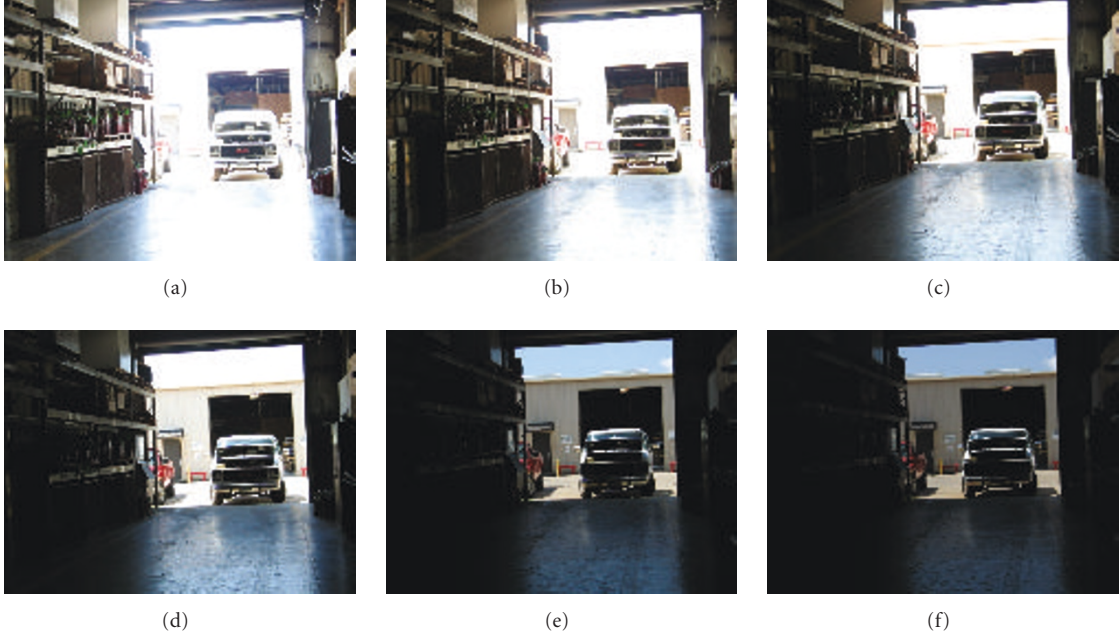(A3) Geometric and photometric registration parameters are estimated jointly.

FIGURE 8: Six images of "Facility II" data set that includes 31 images are displayed here. Exposure durations of (a)–(f) are 1/25, 1/50, 1/100, 1/200, 1/400, and 1/800 seconds, respectively.
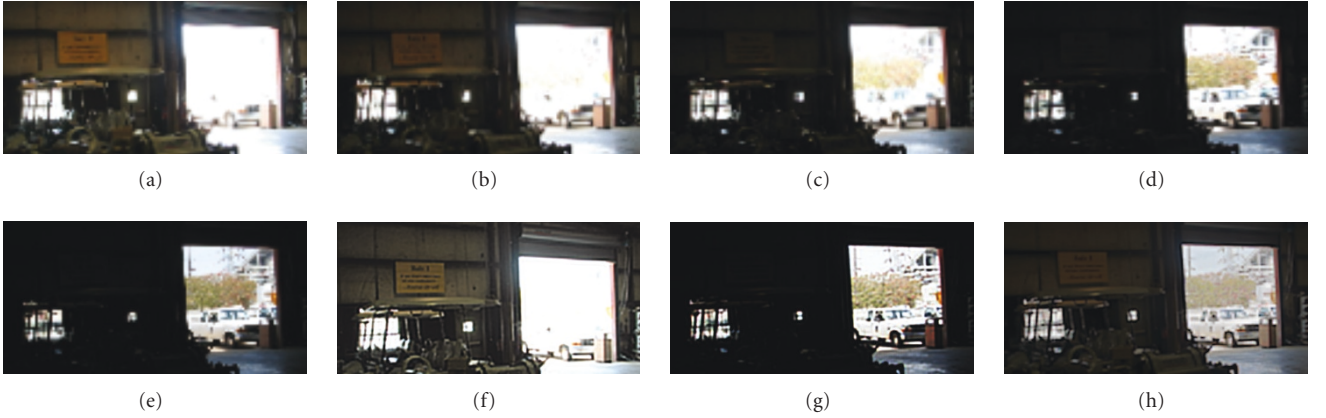

FIGURE 9: Cropped regions of observation and SR results: (a)–(e) input images; (f) SR when (a) is the reference image; (g) SR when (e) is the reference image; (h) SR using the technique presented in Section 3.2.

There are few algorithms that can be utilized for these approaches. In [27], an exposure-insensitive motion estimation algorithm based on the Lucas-Kanade technique is proposed to estimate motion vectors at each pixel. Although this method can be used to estimate large and dense motion field, it has the downside that it requires preknowledge of the CRF. Another exposure-insensitive algorithm is proposed in [28]. It is based on bitmatching on binary images. Although it does not require knowing CRF in advance, the algorithm is limited to global translational motion. In [17], an IMF estimation algorithm that does not require geometric registration is proposed. It is based on the idea that histogram specification gives the intensity mapping between two images when

there is no saturation or significant geometric misalignment. And finally in [29], a joint geometric and photometric registration algorithm is proposed. There, the problem is formulated as a global parameter estimation, where the parameters jointly represent geometric transformation, exposure rate, and CRF. Two potential problems associated with this approach are (1) getting stuck at a local minimum and (2) limitation of using parametric CRF.

We take approach (A1) in our experiments. This is also the approach in [13]. References [5, 12] take the same approach except for the photometric model. For geometric registration, we use a feature-based algorithm, which requires robust exposure-insensitive feature extraction and matching.

FIGURE 10: Cropped regions of observation and SR results: (a)–(d) input images; (e) SR when (d) is the reference image; (f) SR when (a) is the reference image; (g) SR using the technique presented in Section 3.2.
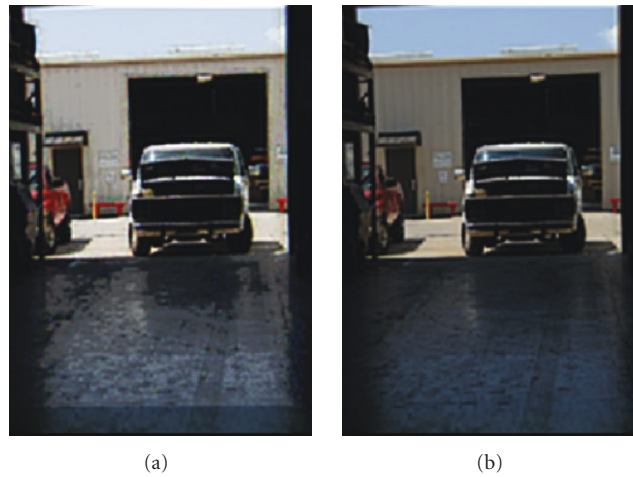

FIGURE 11: Comparison of weighting function during spatial resolution enhancement. The lowest exposed image is chosen as reference. (a) SR reconstruction using identity weight, (b) SR reconstruction using a hat function as weight.

In our experiments, feature points are first extracted using the Harris corner detector [30]. Although the Harris corner detector is not invariant to illumination changes in general, it worked well in our experiments. These feature points are matched using normalized cross-correlation, which is insensitive to contrast changes. The RANSAC method [31] is then used to eliminate the outliers and estimate the homographies. After geometric registration comes photometric registration. There are various methods available in the literature to estimate IMF and CRF as we discussed earlier. In our experiments, we use [19] to estimate IMF, CRF, and the exposure rate.

5. EXPERIMENTS AND RESULTS

We conducted experiments to demonstrate the proposed SR algorithms. (A Matlab toolbox can be downloaded from [32].) We captured two data sets with a handheld digital camera. These data sets are shown in Figures 7 and 8. The resolution enhancement factor is four and the number of iterations was set to two in all experiments. The PSF is taken as a Gaussian window of size $[7 \times 7]$ and of variance 1.7. The results are shown in Figures 9 and 10. For the spatial-only enhancement approach, we did experiments when the reference is chosen as an overexposed image and also when it is chosen

as an underexposed image to show the robustness of the algorithm. For the irradiance-domain spatial and dynamic range enhancement approaches, we created an initial estimate by applying a standard HDR image construction algorithm [9]. The initial estimate is then updated iteratively.

For comparison purposes, we provided cropped regions of results and transformed input images in Figure 9. Figures 9(a), 9(b), 9(c), 9(d), 9(e) are the bilinearly interpolated observations with different exposure rates chosen from the 22 input images. Each observation contains a different portion of the existing tonal range. Figure 9(f) is the SR result obtained when the overexposed image, (Figure 9(a)), is chosen as the reference image. Comparison of Figures 9(a) and 9(f) shows the improvement in resolution. Similarly, Figure 9(g) is obtained when the underexposed image, (Figure 9(e)), is set as the reference image. The resolution enhancement is again clear. Figure 9(h) is the result of the resolution and dynamic-range enhancement algorithm. Notice that both spatial resolution and dynamic range are improved. (Note that the result of an HDR algorithm would have higher dynamic range than a standard display or printing device. Therefore, an HDR image should be compressed in range to output in such LDR devices. There are complex display algorithms [26]. In this paper, we used a simple gamma correction to display the result. The gamma correction parameter is 0.5.) Figure 10 shows the results for the second data set. The discussion is parallel to the discussion of first data set, therefore, it is excluded for conciseness.

Finally, we wanted to test the effect of the weighting function in SR reconstruction. Figures 11(a) and 11(b) aim to increase both spatial resolution and dynamic range, and differ only in their weighting function. Figure 11(a) shows SR result using a unity weight. Notice the loss of information in details and color. Color artifacts occur in this case as the saturated pixels are not handled properly. Strips on the warehouse can hardly be observed and the sky color is washed out due to fusion with saturated residuals. There is also contouring artifact. Figure 11(b) shows the result using the proposed hat function for weighting. Texture and colors are preserved compared to Figure 11(a).

6. CONCLUSIONS

In this paper, we showed how to do SR when the photometric characteristics of the input images are not identical. We showed two possible approaches, one of them enhancing spatial resolution only, and the other enhancing spatial resolution and dynamic range jointly. We demonstrated that nonlinear photometric modeling should be preferred to affine photometric modeling. We also discussed that an appropriate weighting function is necessary to handle saturation. Other SR reconstruction techniques can be modified and applied as long as an appropriate photometric registration is included.

Although geometric registration is a complicated task for differently exposed images, we achieved a success using feature-based registration without the need of CRF. A sequential approach is useful: similarly exposed images would produce similar features; therefore, correct geometric registration would be easier to estimate among similarly exposed images compared to images with large exposure differences. Therefore, one may find the homographies among similarly exposed images, and then combine the homographies to find the homography between any two images. In our experiments, we chose a reference image from the middle of the tonal range. Homographies of input images are found with respect to this reference image. The homography between any two of the input images can then be found by multiplying the corresponding homography matrices. Photometric registration is trivial after the geometric registration.

In this paper, we considered static scenes only. Estimation of motion parameters for nonstatic scenes is left as a future work. Also, we only considered global photometric changes. In experiments, we only considered the exposure rate change which acts globally on image. In general, a dense photometric model is necessary to handle local photometric changes. That is, accurate geometric and photometric registrations of photometrically different image certainly require further research.

REFERENCES

[1] MotionDSP, April 2007, http://www.motiondsp.com/.

[2] QELabs, April 2007, http://www.qelabs.com/.

[3] S. C. Park, M. K. Park, and M. G. Kang, "Super-resolution image reconstruction: a technical overview," *IEEE Signal Processing Magazine*, vol. 20, no. 3, pp. 21–36, 2003.

[4] S. Chaudhuri, Ed., *Super-Resolution Imaging*, Springer, Berlin, Germany, 2001.

[5] D. Capel, *Image Mosaicing and Super-Resolution*, Springer, Berlin, Germany, 2004.

[6] S. Farsiu, D. Robinson, M. Elad, and P. Milanfar, "Advances and challanges in super-resolution," *International Journal of Imaging Systems and Technology*, vol. 14, no. 2, pp. 47–57, 2004.

[7] S. Borman and R. L. Stevenson, "Super-resolution from image sequences: a review," in *Proceedings of the Midwest Symposium on Circuits and Systems*, vol. 5, pp. 374–378, Notre Dame, Ind, USA, April 1998.

[8] E. Reinhard, G. Ward, S. Pattanaik, and P. Debevec, *High Dynamic Range Imaging: Acquisition, Display, and Image-Based Lighting*, Morgan Kaufmann, San Francisco, Calif, USA, 2006.

[9] P. E. Debevec and J. Malik, "Recovering high dynamic range radiance maps from photographs," in *Proceedings of the 24th Annual Conference on Computer Graphics and Interactive Techniques (SIGGRAPH '97)*, pp. 369–378, Los Angeles, Calif, USA, August 1997.

[10] S. Mann and R. W. Picard, "Being 'undigital' with digital cameras: extending dynamic range by combining differently exposed pictures," in *Proceedings of the 48th IS&T's Annual Conference*, pp. 442–448, Washington, DC, USA, May 1995.

[11] M. A. Robertson, S. Borman, and R. L. Stevenson, "Dynamic range improvement through multiple exposures," in *Proceedings of IEEE International Conference on Image Processing (ICIP '99)*, vol. 3, pp. 159–163, Kobe, Japan, October 1999.

[12] D. Capel and A. Zisserman, "Computer vision applied to super resolution," *IEEE Signal Processing Magazine*, vol. 20, no. 3, pp. 75–86, 2003.

[13] B. K. Gunturk and M. Gevrekci, "High-resolution image reconstruction from multiple differently exposed images," *Signal Processing Letters*, vol. 13, no. 4, pp. 197–200, 2006.

[14] A. Litvinov and Y. Y. Schechner, "Radiometric framework for image mosaicking," *Journal of the Optical Society of America A*, vol. 22, no. 5, pp. 839–848, 2005.

[15] D. Hasler and S. Süsstrunk, "Mapping colour in image stitching applications," *Journal of Visual Communication and Image Representation*, vol. 15, no. 1, pp. 65–90, 2004.

[16] S. K. Nayar, K. Ikeuchi, and T. Kanade, "Shape from interreflections," *International Journal of Computer Vision*, vol. 6, no. 3, pp. 173–195, 1991.

[17] M. D. Grossberg and S. K. Nayar, "Determining the camera response from images: what is knowable?" *IEEE Transactions on Pattern Analysis and Machine Intelligence*, vol. 25, no. 11, pp. 1455–1467, 2003.

[18] S. Mann, C. Manders, and J. Fung, "Painting with looks: photographic images from video using quantimetric processing," in *Proceedings of the 10th ACM International Conference on Multimedia (MULTIMEDIA '02)*, pp. 117–126, Juan les Pins, France, December 2002.

[19] S. Mann and R. Mann, "Quantigraphic imaging: estimating the camera response and exposures from differently exposed images," in *Proceedings of IEEE Computer Society Conference on Computer Vision and Pattern Recognition (CVPR '01)*, vol. 1, pp. 842–849, Kauai, Hawaii, USA, December 2001.

[20] T. Mitsunaga and S. K. Nayar, "Radiometric self calibration," in *Proceedings of IEEE Computer Society Conference on Computer Vision and Pattern Recognition (CVPR '99)*, vol. 1, pp. 374–380, Fort Collins, Colo, USA, June 1999.

[21] Y. Tsin, V. Ramesh, and T. Kanade, "Statistical calibration of CCD imaging process," in *Proceedings of the 8th IEEE International Conference on Computer Vision (ICCV '01)*, vol. 1, pp. 480–487, Vancouver, BC, Canada, July 2001.

[22] S. Mann, "Comparametric equations with practical applications in quantigraphic image processing," *IEEE Transactions on Image Processing*, vol. 9, no. 8, pp. 1389–1406, 2000.

[23] A. J. Patti, M. I. Sezan, and A. M. Tekalp, "Superresolution video reconstruction with arbitrary sampling lattices and nonzero aperture time," *IEEE Transactions on Image Processing*, vol. 6, no. 8, pp. 1064–1076, 1997.

[24] R. R. Schultz and R. L. Stevenson, "Extraction of high-resolution frames from video sequences," *IEEE Transactions on Image Processing*, vol. 5, no. 6, pp. 996–1011, 1996.

[25] M. Irani and S. Peleg, "Improving resolution by image registration," *CVGIP: Graphical Models & Image Processing*, vol. 53, no. 3, pp. 231–239, 1991.

[26] R. Fattal, D. Lischinski, and M. Werman, "Gradient domain high dynamic range compression," *ACM Transactions on Graphics*, vol. 21, no. 3, pp. 249–256, 2002.

[27] S. B. Kang, M. Uyttendaele, S. Winder, and R. Szeliski, "High dynamic range video," *ACM Transactions on Graphics*, vol. 22, no. 3, pp. 319–325, 2003.

[28] G. Ward, "Fast, robust image registration for compositing high dynamic range photographs from hand-held exposures," *Journal of Graphics Tools*, vol. 8, no. 2, pp. 17–30, 2003.

[29] F. M. Candocia, "Jointly registering images in domain and range by piecewise linear comparametric analysis," *IEEE Transactions on Image Processing*, vol. 12, no. 4, pp. 409–419, 2003.

[30] C. G. Harris and M. Stephens, "A combined corner and edge detector," in *Proceedings of the 4th Alvey Vision Conference*, pp. 147–151, Manchester, UK, August-September 1988.

[31] M. A. Fischler and R. C. Bolles, "Random sample consensus: a paradigm for model fitting with applications to image analysis and automated cartography," *Communications of the ACM*, vol. 24, no. 6, pp. 381–395, 1981.

[32] M. Gevrekci and B. K. Gunturk, "Matlab user interface for super resolution image reconstruction for illumination varying and Bayer pattern images," April 2007, http://www.ece.lsu.edu/ipl/Demos.html.

Murat Gevrekci received his B.S. degree in electrical engineering from Bilkent University, Ankara, Turkey, in 2004, and the M.S. degree in electrical and computer engineering from Louisiana State University, Baton Rouge, La, in 2006. He is currently pursuing his Ph.D. degree at Louisiana State University. His research interests include image/video processing, parallel image processing, and computer vision. He published several peer-reviewed articles and served as a Technical Reviewer for various journals in the field of signal processing. He is a Student Member of the IEEE.

Bahadir K. Gunturk received his B.S. degree in electrical engineering from Bilkent University, Ankara, Turkey, in 1999, and M.S. and Ph.D. degrees in electrical engineering from Georgia Institute of Technology, Atlanta, Ga, in 2001 and 2003, respectively. He is currently an Assistant Professor at Louisiana State University, Baton Rouge, La. His main research interest is computer vision. He is a Member of the IEEE.